Helical resonant transport and purified amplification at an exceptional point

K. L. Zhang, L. Jin,* and Z. Song†
School of Physics, Nankai University, Tianjin 300071, China

We propose an application of a parity-time symmetric non-Hermitian Su-Schrieffer-Heeger (SSH) model by embedded it in a two-dimensional square lattice tube. The coalescence state at the exceptional point of non-Hermitian SSH model is chiral and selectively controls helical transport and amplification. Two typical helicity-dependent scattering dynamics are observed. If the incidence has an identical helicity with the embedded non-Hermitian SSH model, we observe a perfect transmission without reflection. However, if the incidence has an opposite helicity with the embedded non-Hermitian SSH model, except for a full transmission, we observe an amplified transmission with different helicity from the incidence; but the amplified reflection has identical helicity with the incidence. These intriguing features are completely unexpected in Hermitian system. Moreover, the helical amplification at high efficiency can be triggered by an arbitrary excitation. The different dynamics between incidences with opposite helicities are results of unidirectional tunneling, which is revealed to be capable of realizing without introducing magnetic field. We give a discussion about the helical dynamics under system imperfections. Our findings open a direction in all-optical device and provide perspectives in non-Hermitian transport.

arXiv:1907.12829v2 [cond-mat.mes-hall] 3 Oct 2019

I. INTRODUCTION

Nowadays non-Hermitian physics has emerged as a versatile platform for the exploring of functional devices that are absent or difficult to realize in Hermitian regime [1–18]. The passive and active $\mathcal{PT}$-symmetric non-Hermitian systems with balanced gain and loss are investigated theoretically and experimentally in various setups in optics [19–26]. The non-Hermiticity induces nonunitary dynamic including the power oscillation [10, 12] and the unidirectional invisibility [13–15]. However, the $\mathcal{PT}$ symmetry protects the symmetry of transmission [27–30]. An ideal building block possessing asymmetric transmission is the asymmetric dimer with an unequal hopping strength [31]. Asymmetric hopping strength can be realized in coupled microring resonators with synthetic imaginary gauge fields in photonics [32, 33]. Moreover, asymmetric transmission is possible under gain and loss associated with effective magnetic flux [34–40]. Nonreciprocal photonics in the non-Hermitian physics are revealed to be useful for the applications in optics [40–45].

Non-Hermitian system at exceptional point (EP) has a coalescence state [6, 46]. We propose an application of the $\mathcal{PT}$-symmetric non-Hermitian Su-Schrieffer-Heeger (SSH) model at the EP [47–53], which exhibits unidirectionality without the assistance of magnetic field. The unidirectionality leads to the helicity dependent dynamics of wave propagation. The non-Hermitian SSH ring is embedded in a square lattice tube center as a scattering center. The wave propagation of different incidences are studied. The non-Hermitian SSH ring at EPs has a coalescence state, which is chiral due to the chirality of EP and coincides with one of the two degenerate zero modes of a uniform ring. Thus, the non-Hermitian SSH ring engineered at the EPs results in helical transport. The non-Hermitian SSH ring at the EP leads to two typical helicity-dependent scattering behaviors: (i) zero transverse bandwidth perfect transmission without reflection; (ii) amplified zero transverse bandwidth interfered transmission with reflection. In the later case, except for a resonant transmission, part of the transmission after scattering has opposite helicity with the incidence; and the reflection has identical helicity with the incidence. This dramatically differs from the traditional helical scattering that transmission after scattering has identical helicity with the incidence, but the reflection has opposite helicity with the incidence. These features are useful for the control of helical transport and amplification. We also show that the helical amplification can be triggered by an arbitrary excitation at high efficiency.

This paper is organized as follows. In Sec. II, we present the square lattice tube model embedded with a non-Hermitian SSH ring. In Sec. III, we discuss the unidirectional hopping and show the helical dependent dynamics under the influence of the non-Hermitian SSH ring. In Sec. IV, we demonstrate the purification and amplification for a single-site excitation. In Sec. V, we investigate the system with imperfections and discuss the possible experimental realization. In Sec. VI, we summarize our findings.

II. CHIRAL SCATTERING CENTER

We consider a non-Hermitian engineering of the tube, the schematic is illustrated in Fig. 1(a). A non-Hermitian SSH ring is embedded in the center ($j = 0$) of the tube [49, 50, 52]. The non-Hermitian SSH ring has staggered coupling along the y direction, and the gain and loss are staggered. The dynamics in the tube can be considered as a scattering problem. Before we handling the problem of chiral scattering center, we first discuss a uniform square lattice tube without any impurity; and then discuss the

* jinliang@nankai.edu.cn
† songtc@nankai.edu.cn

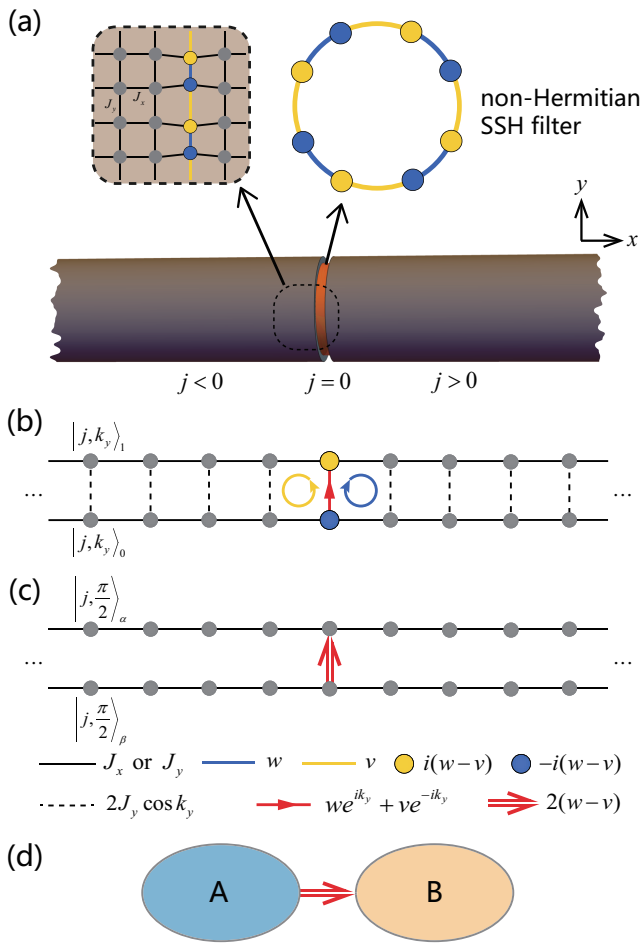

FIG. 1. (a) Schematic of the infinite lattice tube with a non-Hermitian SSH ring embedded in the center. The SSH ring is set at the EP. (b) Ladder lattice of the Hamiltonian [Eq. (4)] in the k_y momentum space. The scattering center generates two opposite magnetic fluxes in the two neighbor plaquettes. (c) Schematic of the equivalent ladder of Eq. (8). (d) Schematic of two Hermitian subsystems A and B with unidirectional hopping (red double arrow). (c) is a concrete example of (d).

non-Hermitian SSH model and its zero energy eigenstates at the EP.

The uniform infinite square lattice tube without any impurity has infinite sites in the x direction, and the supported momentum in the x direction is continuous in the region $k_x \in [-\pi, \pi]$. The tube is periodic along the y direction and has total $2M$ sites, and the supported momentum in the y direction is discrete $k_y = n\pi/M$ (integer $n = 1, 2, ..., 2M$). The (unnormalized) eigenstate of the uniform square lattice tube without any impurity is given by

$$|\Psi\rangle = \frac{1}{\sqrt{2M}} \sum_{j=-\infty}^{\infty} e^{ik_x j} \sum_{l=1}^{2M} e^{ik_y l} |j, l\rangle , \tag{1}$$

which is a plane wave steady-state scattering solution in

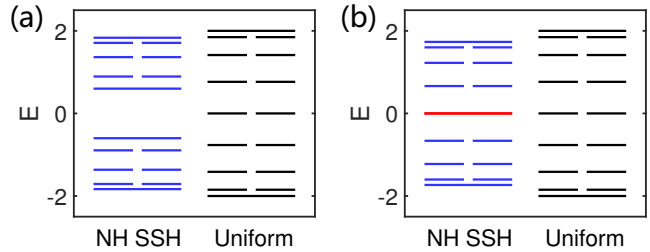

FIG. 2. Energy levels (solid lines) of the non-Hermitian SSH ring and the uniform ring. The non-Hermitian SSH ring has staggered coupling w and v; and stagger gain and loss $\pm i\gamma$. The uniform ring has uniform coupling J. (a) $\gamma = 0.8$. (b) $\gamma = 1$. Other parameters are $w = 1.5$, $v = 0.5$, and $J = 1$. Both ring sizes are 16. The red line in (b) represents the coalesced energy level, other levels in (b) and all levels in (a) are all mismatched.

the x direction. In the eigenstate of the uniform square lattice tube $|\Psi\rangle$, $|j, l\rangle$ is the Wannier representation [54, 55]; j (l) is the index of the lattice in the x (y) direction; and $|j, l\rangle$ stands for the Wannier state localized at lattice site (j, l) of the lattice tube.

The eigen energies of the non-Hermitian SSH ring are significantly different from the eigen energies of the uniform ring. The energy levels of the non-Hermitian SSH ring and the uniform ring are compared in Fig. 2(a); correspondingly, the supported discrete momenta k_y are mismatched. Consequently, the incidences in the tube can not pass the non-Hermitian SSH ring center and are blocked. However, if the non-Hermitian SSH ring H_{SSH} is engineered at the EP, it has a coalescence eigenstate with zero energy. The coalesced zero mode is

$$|\psi_-\rangle = \frac{1}{\sqrt{2M}} \sum_{l=1}^{2M} e^{-il\pi/2} |0, l\rangle . \tag{2}$$

The intriguing feature of the coalescence eigenstate $|\psi_-\rangle$ is that it is identical to one of the two degenerate zero energy eigenstates of the uniform ring (at the momentum $k_y = \pm\pi/2$) as elaborated in Fig. 2(b). For the Hermitian conjugation SSH ring $H^\dagger_{\text{SSH}}$, it differs from H_{SSH} only in the sense that the gain and loss are interchanged. $H^\dagger_{\text{SSH}}$ is also at the EP and supports a coalescence zero energy eigenstate in the form of

$$|\psi_+\rangle = \frac{1}{\sqrt{2M}} \sum_{l=1}^{2M} e^{+il\pi/2} |0, l\rangle . \tag{3}$$

Notably, the two coalescence eigenstates in H_{SSH} and $H^\dagger_{\text{SSH}}$ are the two degenerate zero modes of the uniform ring, being orthogonal $\langle\psi_-|\psi_+\rangle = 0$. The two coalescence eigenstates possess opposite chiralities classified by the type of EP [6, 46, 56–58]. The non-Hermitian SSH ring H_{SSH} engineered at the EP only supports the resonant transmission for the incident wave with one of two momenta $k_y = \pm\pi/2$.

The non-Hermitian SSH ring in the tube is regarded as the scattering center; the semi-infinite tubes coupled to the non-Hermitian SSH ring are regarded as the leads. Notably, the leads are translational invariant by shifting every one site in the y direction; however, the non-Hermitian SSH ring center is translational invariant by shifting every two sites in the y direction. This is an important feature for the design of helical transport in this paper.

To comprehensively address the scattering inside the tube, we write down the tube Hamiltonian in the momentum space $H = \sum_{k_y} H_{k_y}$. H_{k_y} describes a ladder system as schematically illustrated in Fig. 1(b). The Hamiltonian in the momentum subspace k_y reads

$$\begin{aligned} H_{k_y} = J_x \sum_{j=-\infty}^{\infty} \sum_{\lambda=1,0} & |j-1,k_y\rangle_{\lambda\lambda} \langle j,k_y| \\ & +2J_y \cos k_y \sum_{j\neq 0, j=-\infty}^{\infty} |j,k_y\rangle_{10} \langle j,k_y| \\ & + \left(we^{ik_y} + ve^{-ik_y}\right) |0,k_y\rangle_{10} \langle 0,k_y| + \text{H.c.} \\ & -i(w-v)(-1)^{\lambda} \sum_{\lambda=1,0} |0,k_y\rangle_{\lambda\lambda} \langle 0,k_y| , \end{aligned} \tag{4}$$

The Fourier transformations applied to the square lattice tube is $|j,k_y\rangle_{\lambda} = M^{-1/2} \sum_{l=1}^{M} e^{ik_y(2l-\lambda)} |j,2l-\lambda\rangle$, where $\lambda = 1,0$ and $k_y = n\pi/M$, $(n = 1,2,...,M)$. H_{k_y} with different momenta commute

$$[H_{k_y}, H_{k'_y}] = 0. \tag{5}$$

This means that H can be decomposed into M-fold independent sub-Hamiltonians. The ladder H_{k_y} has a non-Hermitian dimer embedded in the center. Remarkably, any distortion $w \neq v$ generates two opposite effective magnetic fluxes in the two plaquettes with gain and loss.

An interesting situation is when the ladder has zero effective magnetic fluxes at $k_y = \pi/2$ although the presence of nonreciprocal Hermitian coupling $i\,(w-v)$ with a Peierls phase factor $i = e^{i\pi/2}$. This structure is equivalent to the ladder with asymmetric coupling in Fig. 1(c) without employing effective magnetic flux [59, 60]. The asymmetric coupling is physical, the asymmetric coupling amplitudes for photons tunneling in the opposite directions is proposed in the coupled ring resonator array [32, 33]. From the analysis of the $k_y = \pi/2$ subspace, we can obtain the previous conclusion discussed.

III. UNIDIRECTIONAL TUNNELING AND HELICAL RESONANT TRANSPORT

In the $k_y = \pi/2$ subspace, term with coupling $2J_y \cos k_y$ vanish, and the ladder Hamiltonian in Eq. (4)

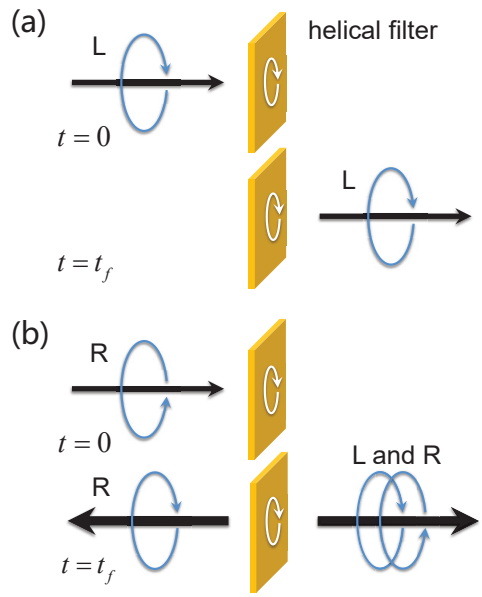

FIG. 3. Schematic of the helical transport. The helical filter is the SSH ring at EP. (a) Perfect transmission with zero transverse bandwidth for incident wave possessing identical helicity with the SSH ring helical filter. (b) Full transmission associating with out going wave for incidence possessing opposite helicity with the SSH ring helical filter.

reduces to the form of

$$\begin{aligned} H_{\pi/2} = J_x \sum_{j=-\infty}^{\infty} \sum_{\lambda=1,0} & |j-1,\pi/2\rangle_{\lambda\lambda} \langle j,\pi/2| \\ & +i\,(w-v)\,|0,\pi/2\rangle_{10} \langle 0,\pi/2| + \text{H.c.} \\ & -i(w-v)(-1)^{\lambda} \sum_{\lambda=1,0} |0,\pi/2\rangle_{\lambda\lambda} \langle 0,\pi/2| . \end{aligned} \tag{6}$$

Taking the unitary transformation

$$\begin{aligned} |j,\pi/2\rangle_{\alpha} &= \frac{1}{\sqrt{2}} \left(|j,\pi/2\rangle_1 - |j,\pi/2\rangle_0\right), \\ |j,\pi/2\rangle_{\beta} &= \frac{-i}{\sqrt{2}} \left(|j,\pi/2\rangle_1 + |j,\pi/2\rangle_0\right), \end{aligned} \tag{7}$$

with $j = 0, \pm1, \pm2, ...$, the Hamiltonian can be rewritten in the form of

$$\begin{aligned} H_{\pi/2} = J_x \sum_{j=-\infty}^{\infty} & \left(|j-1,\pi/2\rangle_{\alpha\alpha} \langle j,\pi/2| \right. \\ & \left. + |j-1,\pi/2\rangle_{\beta\beta} \langle j,\pi/2|\right) + \text{H.c.} \\ & +2\,(w-v)\,|0,\pi/2\rangle_{\alpha\beta} \langle 0,\pi/2| , \end{aligned} \tag{8}$$

which is schematically illustrated in Fig. 1(c). We note that the non-Hermiticity of $H_{\pi/2}$ only arises from the unidirectional hopping term $2\,(w-v)\,|0\rangle_{\alpha} \langle 0|_{\beta}$ and $H_{\pi/2}$ still has parity symmetry. The composed asymmetric coupling takes the advantages of the two leads structure, which differs from other cases in the literatures [34–40].

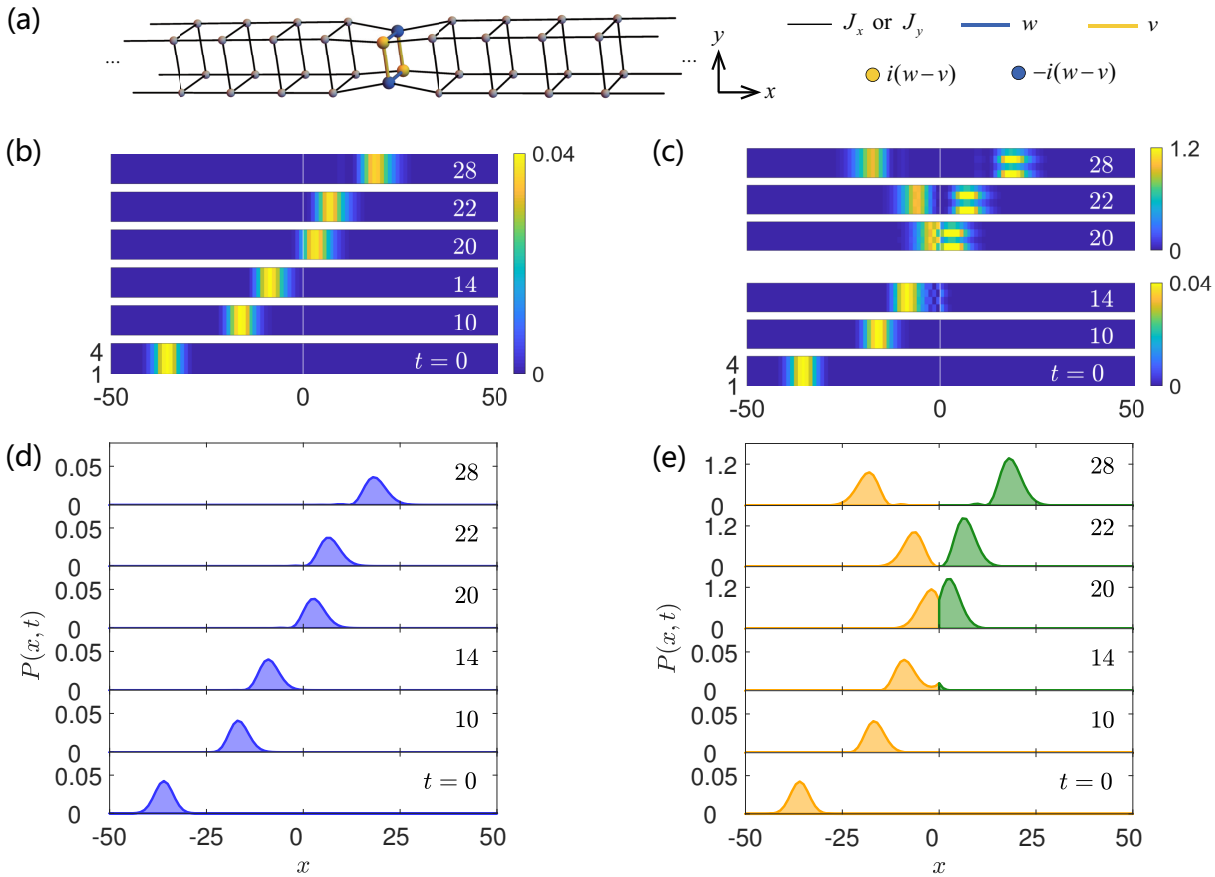

FIG. 4. (a) Non-Hermitian lattice tube with $M = 2$. Snapshots of the intensity at various time moments for two typical initial excitations: (b) Perfect transmission of Gaussian profile $\left|\Psi_{\mathrm{G}}^{-}(0)\right\rangle$ with identical helicity of the filter; (c) Gaussian profile $\left|\Psi_{\mathrm{G}}^{+}(0)\right\rangle$ with opposite helicity of the filter. The interference pattern at $x > 0$ in (c) shows light and dark areas, which indicate the interference of transmitted excitation with opposite helicities [see Eq. (11)]. (d) and (e) are the intensity distribution in the y direction for (b) and (c), respectively. The blue (gold) area represents the output with the identical (opposite) helicity of the filter, while the green area represents the output with two helicities. Other parameters of the initial excitation are $\alpha_{\mathrm{w}} = 0.3$, $k_x = -\pi/2$ and $N_{\mathrm{c}} = -35$ and for the system are $J_x = J_y = J = 0.25$, $w = 1.5$, $v = 0.5$ and the time is in unit of J^{-1}.

A tight-binding network is constructed topologically by the sites and various connections between them. There are three types of basic non-Hermitian clusters leading to the non-Hermiticity of a discrete non-Hermitian system: i) complex on-site potential denoted as $(V + i\gamma)\left|l\right\rangle\left\langle l\right|$; ii) non-Hermitian dimer denoted as $e^{i\varphi}(\left|l\right\rangle\left\langle j\right| + \left|j\right\rangle\left\langle l\right|)$, and iii) asymmetric hopping amplitude dimer denoted as $\mu\left|l\right\rangle\left\langle j\right| + \nu\left|j\right\rangle\left\langle l\right|$ $(\mu \neq \nu)$, where $V, \gamma, \varphi, \mu, \nu$ are real numbers. The asymmetric hopping induces imaginary magnetic flux and has been used in modeling a delocalization phenomenon [61]. The unidirectional hopping is defined as $\mu\nu = 0$, which is an extreme non-Hermitian term, only allows the particle tunneling from A to B.

The unidirectional hopping we encounter here is a basic non-Hermitian element in the context of tight-binding network, which leads to unidirectional tunneling between two Hermitian subsystems A and B [Fig. 1(d)]: On the one hand, when an initial state is set in subsystem B, the particle is always confined in B and thus the Dirac probability is conservative. On the other hand, when an initial state is set in subsystem A, the particle can tunnel to B and thus the Dirac probability is not conservative. Subsystem can be regarded as a conditional invariant subspace, which is an exclusive feature of a non-Hermitian system. These features can be seen by considering the scattering problem of Hamiltonian Eq. (8).

We take the momentum $k_y = \pm\pi/2$ as an inner degree of freedom; $k_y = -\pi/2$ indicates the circling toward the positive direction of y, thus, an angular momentum associated with $k_y = -\pi/2$ is toward the negative direction of x; in contrast, an angular momentum associated with $k_y = \pi/2$ is toward the positive direction of x. For incidence with $k_y = -\pi/2$ $(k_y = \pi/2)$ moving toward the positive direction of x, the direction of angular momentum associated with k_y is opposite (identical) to its propagation direction along x, thus, we refer to the helicity as the left-handed (right-handed).

Now we consider the scattering problem for a unidirectional scattering center, which is exactly solvable and is of significant not only for the non-Hermitian physics

but also for applications in optics. A direct motivation is that the equivalent Hamiltonian of the present Hamiltonian in an invariant subspace is a concrete example with unidirectional tunneling. Two solutions of the scattering wave function in the subspace $H_{\pi/2}$ can be obtained by the Bethe ansatz method (see Appendix A). For incidence with momentum k_x in the x direction, the resonant transmission solution is

$$\left|\psi_{k_x}^{L}\right\rangle = \frac{1}{\sqrt{2M}} \sum_{j=-\infty}^{\infty} \sum_{l=1}^{M} e^{ik_x j}(-1)^l \left(|j, 2l-1\rangle - i\,|j, 2l\rangle\right), \tag{9}$$

and the interfered transmission solution is

$$\left|\psi_{k_x}^{R}\right\rangle = \frac{1}{\sqrt{2M}} \sum_{j=-\infty}^{\infty} \sum_{l=1}^{M} [e^{ik_x j}(-1)^l \left(|j, 2l-1\rangle + i\,|j, 2l\rangle\right) + A_{k_x} e^{ik_x|j|}(-1)^l \left(|j, 2l-1\rangle - i\,|j, 2l\rangle\right)], \tag{10}$$

with $A_{k_x} = (v-w)\,/\,(J_x \sin k_x)$ the k_x-dependent amplified amplitude.

Two solutions have the following implications when we consider incidences with opposite helicities. (i) $\left|\psi_{k_x}^{L}\right\rangle$ indicates a perfect resonant transmission for the $(|j, 2l-1\rangle - i\,|j, 2l\rangle)$-type (left-handed) incident wave, where $-i$ indicates the momentum $k_y = -\pi/2$. (ii) $\left|\psi_{k_x}^{R}\right\rangle$ indicates a combination of perfect resonant transmission and an equal amplitude $(|j, 2l-1\rangle - i\,|j, 2l\rangle)$-type out going waves with k_x-dependent amplitude for the $(|j, 2l-1\rangle + i\,|j, 2l\rangle)$-type (right-handed) incident wave, where $+i$ indicates the momentum $k_y = +\pi/2$. The amplitude is inversely proportional to the group velocity $2J_x \sin k_x$ of the incidence, and diverges only for zero group velocity. In the region $j > 0$, we have

$$\left|\langle j, 2l - \lambda\,|\psi_{k_x}^{R}\rangle\right|^2 = \frac{1}{2M}\left[(-1)^{\lambda} + \frac{w-v}{J_x \sin k_x}\right]^2, \tag{11}$$

which indicates an interference pattern along the transverse direction (y direction). In particular, for $\sin k_x = \pm(w-v)/J_x$, it exhibits transverse standing-wave mode, which indicates that the transmitted waves only appear in the tube leads embedded the blue sites or the yellow sites.

So far we have given a complete analysis of the scattering problem for the incidence with transverse wave vector $k_y = \pm\pi/2$. For other incidences with $k_y \neq \pm\pi/2$, the coalescing state of the non-Hermitian SSH ring is a forbidden channel due to the mismatch of the transverse momentum k_y. Other channel in the scattering center can also be eliminated adiabatically at large staggered coupling $w, \nu \gg J_x, J_y$, resulting in near perfect reflection. As a temporary summary, we can conclude that the present system allows the coexistence of two types of helical resonant transport: (i) zero transverse bandwidth perfect transmission, (ii) zero transverse bandwidth amplified transmission and reflection. These phenomena are schematically simulated in Fig. 3.

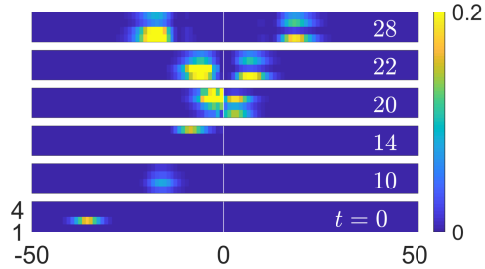

FIG. 5. Snapshots of the intensity for single-site excitation in the y direction. The parameters of the initial excitation are $\alpha_{\rm w} = 0.3$, $k_x = -\pi/2$ and $N_{\rm c} = -35$, and of the system are $J_x = J_y = J = 0.25$, $w = 1.5$, $v = 0.5$. The time unit is J^{-1}.

To verify and demonstrate the performance of the proposed scheme, we simulate the time evolutions for both two typical cases. We consider two kinds of Gaussian wave packet with opposite helicities as the initial excitation

$$\left|\Psi_{\rm G}^{\pm}(0)\right\rangle = \Omega^{-\frac{1}{2}} \sum_{j=-\infty}^{\infty} \sum_{l=1}^{2M} e^{-\frac{\alpha_{\rm w}^2 (j-N_{\rm c})^2}{2}} e^{ik_x j} e^{\pm i\frac{\pi}{2} l}\,|j, l\rangle, \tag{12}$$

where $\Omega = 2M\sqrt{\pi}/\alpha_{\rm w}$ is the normalization constant. The parameter $\alpha_{\rm w}$ determines the width of the Gaussian wavepacket and $N_{\rm c}$ is the initial position of its center. We numerically calculate the evolved wave function $\left|\Psi_{\rm G}^{\pm}(t)\right\rangle = e^{-iHt}\left|\Psi_{\rm G}^{\pm}(0)\right\rangle$ for the system with $M = 2$ [see Fig. 4(a)]. The non-Hermitian SSH ring as the filter is located at the position $x = 0$. We present the numerical results, including the profiles of the evolved excitations and the probability distribution in y direction for the evolved excitations in Figs. 4(b)-(e). We also present the numerical results for the system with $M = 4$ in Fig. B1 (see Appendix B). Both cases verify our predictions.

IV. PURIFICATION AND AMPLIFICATION BY THE HELICAL FILTER

For the incidence possessing an opposite helicity with the non-Hermitian SSH ring filter, the filter generates a $(w-v)/\,(J_x \sin k_x)$ times amplified out going wave possessing both identical and opposite helicities with the filter toward different directions. If $(w-v) \gg J_x$ or k_x approaches to 0 and π, the reflection and transmission beams dominate after the incidence is scattered at the filter.

We first consider an initial single-site excitation in the y direction in comparison with a plane wave excitation in Eq. (12). The filter has the left-handed helicity and the initial excitation is Gaussian in the x direction in the form of

$$|\Psi_{\rm G}(0)\rangle = \Omega^{-\frac{1}{2}} \sum_{j=-\infty}^{\infty} e^{-\frac{\alpha_{\rm w}^2 (j-N_{\rm c})^2}{2}} e^{ik_x j}\,|j, 2\rangle, \tag{13}$$

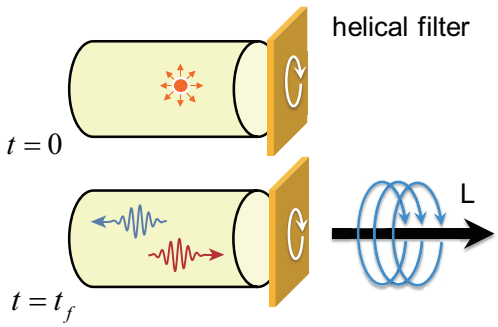

FIG. 6. Schematic of purified amplification triggered by a single-site excitation. Both helical filter and passing wave have the left-handed helicity.

where $\Omega = \sqrt{\pi}/\alpha_{\rm w}$ is the normalization constant. From the simulation in Fig. 5, we notice that the evolved excitation is amplified after being scattered at the filter. In the $x > 0$ region, the light and dark areas as a typical result of interference is observed. This indicates that the output in this region consists of two components with opposite helicities. The single-site excitation in the y direction consists all the possible discrete momentum k_y determined by the size $2M$. Consequently, we notice the spreading of single-site excitation at the moment $t = 10$ before reaching the filter. After scattering, all the components with momentum $k_y \neq \pm\pi/2$ are reflected back to the $x < 0$ region because their energies mismatch the energies of the filter. The component with left-handed helicity ($k_y = -\pi/2$) or right-handed helicity ($k_y = \pi/2$) is resonant with the coalesced zero mode of the filter. The component with left-handed helicity ($k_y = -\pi/2$) is perfect transmitted. However, the component with right-handed helicity ($k_y = \pi/2$), except for a perfect transmission, can induces the right-handed reflected and left-handed transmitted wave due to the gain in the filter; and the right-handed reflected and left-handed transmitted wave are the dominant components after scattering.

Then, we consider a single-site excitation in the tube. The tube has a hard boundary on its left side (Fig. 7), which perfectly reflects all the waves. The left boundary together with the filter form a chamber. For a single-site excitation, the excitation includes the momentum components in the full region of k_x and k_y. However, only wave with right-handed or left-handed helicity ($k_y = \pm\pi/2$) can pass the filter and are amplified with one dominant helicity identical to the filter in the output. The waves with different momentum k_x has different amplified ratio and moving velocity in the x direction. Figure 6 schematically explains the dynamics of a single-site excitation. In Fig. 7, we consider an initial single-site excitation in the chamber. The profiles of the evolved wave functions are simulated. The output wave well demonstrates our description. In Fig. 7(a), the fringes indicate the purified passing waves with left-handed helicity (being amplified and then being dominant) similar as the incidence in Figs. 4(b) and 4(c); the intensity spreading in the x direction indicates the output with different velocities. In Fig. 7(b), the intensities of different helicities as functions of time are depicted. The output after scattered by the helical filter has a dominant left helicity, which possesses identical helicity with the filter.

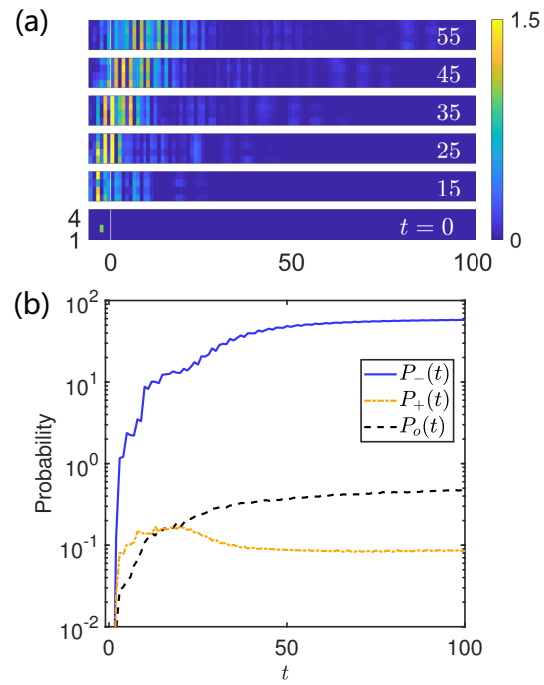

FIG. 7. (a) Snapshots of the intensity of evolved wave for a single-site excitation. The dynamics indicates an amplified single helicity output. The system parameters are $M = 2$, $J_x = J_y = J = 0.25$, $w = 1.5$, $v = 0.5$ and the time unit is J^{-1}. (b) Total transmitted intensity for (a). The blue and gold lines represent the transmitted intensity ($x > 0$) with the left-handed and right-handed helicities, respectively. The black dash line represents the summation of intensities for all the other momentum components.

V. DISCUSSION

In the previous analytical and numerical calculations, the parameters of SSH ring in the system is set at the EP exactly. However, in the experiment, the imperfections of defect or impurity may present; which may drive the non-Hermitian system unstable with exponential increase of excitation intensity. Notably, the zero energy of non-Hermitian SSH ring engineered at the EP is sensitive to the system parameters, and is thus sensitive to the system imperfections. Thus, it is worth to investigate the dynamics in the presence of imperfections or at system parameters deviated from the EP. On the one hand, we consider the influence of imperfections present in all the

parameters of the SSH ring

$$\begin{aligned} w_l &= w + \delta_{w,l}, \\ v_l &= v + \delta_{v,l}, \\ \gamma_l &= w - v + \delta_{\gamma,l}, \end{aligned} \tag{14}$$

where $\delta_{w,l}$, $\delta_{v,l}$, and $\delta_{\gamma,l}$ are all random real numbers within the interval $[-R, R]$ and l is the site index. The numerical simulations for the perfect transmission and interfered transmission simulated in Fig. 4(b) and (c) under $R = 0.01$ and $R = 0.05$ are shown in Fig. 8. We observe that when $R = 0.01$, the dynamics of perfect transmission and interfered transmission are almost unaffected although in the presence of random imperfections; however, when $R = 0.05$, the imperfections apparently affect the wave dynamics. The numerical results show that the dynamics in the system is not sensitive to slight imperfections. The reason is that the imaginary part of the perturbed zero energy is not large enough to exhibit exponential increase of excitation intensity in a limited time region.

On the other hand, when the parameters of the SSH ring are deviated from the EP, the lattice support the bound state [62] with imaginary energy at the large deviation. We numerically investigate the system in Fig. B1(a) (see Appendix B), where the gain and loss for the system is chosen $\pm i\gamma = \pm i(w - v) = \pm i$. We replace γ by $\gamma \to \gamma + \delta$ with a positive small real number δ. The eigenstates of the zero energy levels for the system with $\delta = 0$ are all extended states. Some of them are the coalesced zero energy levels, which are responsible for the helical dynamics. When the deviation from EP is slight, for example $\delta \leqslant 0.01$, though the imaginary energy levels appear, the bound state does not exist and the helical dynamics are almost unaffected. When $\delta = 0.15$, the bound states localized at the SSH ring with imaginary energy are observed. The absence of bound state with imaginary energy explains why the system is stable under slight imperfections.

The 2D square lattice tube is not easily to be realized. However, the experimental realization of quasi-1D systems shown in Fig. 1(b) is ready. The quasi-1D system is essential for the helical dynamics proposed in the square lattice tube. We discuss a possible realization with the coupled resonator array. The quasi-1D system considered in Fig. 1(b) at $k_y = \pi/2$ consists of two uniformly coupled resonator arrays and a $\mathcal{PT}$-symmetric non-Hermitian dimer scattering center with gain and loss $\pm i\,(w - v)$; which can be induced by pumping the doped ions and sticking additional absorption material. The single inter-array nonreciprocal coupling (represented by the red arrow) has a Peierls phase factor $e^{\pm i\pi/2}$ in the front. The Peierls phase can be generated through a path length imbalance method [63]. From the scattering solutions in Eqs. (A10) and (A11) (see Appendix A), we can see that the quasi-1D system support the perfect transmission and interfered transmission; while it can not be used to observe the purified amplification dynamic proposed in the 2D system. The non-Hermitian SSH model

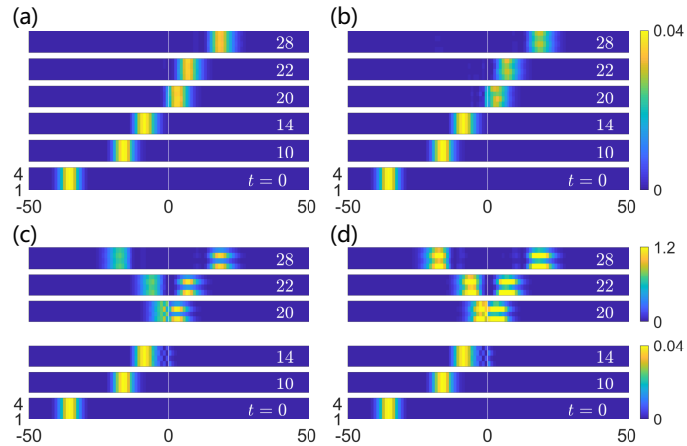

FIG. 8. Dynamics for $M = 2$ system with random disorder in the parameters of the SSH ring. (a, b) Perfect transmission case as comparison with Fig. 4(b). (c, d) Interfered transmission case as comparison with Fig. 4(c). $R = 0.01$ for (a, c) and $R = 0.05$ for (b, d). Other parameters are $\alpha_{\rm w} = 0.3$, $k_x = -\pi/2$ and $N_{\rm c} = -35$ for the initial excitation and $J_x = J_y = J = 0.25$, $w = 1.5$, $v = 0.5$ for the system. The unit of time is J^{-1}.

is a prototypical topological model, further study on the application of other $\mathcal{PT}$-symmetric non-Hermitian topological system [64–66] and topological system with non-Hermitian skin effect [67, 68] will be interesting. All these 1D and quasi-1D systems are ready to be realized in the experiments [69, 70].

The helical dynamics can be observed in a more simple 2D square lattice with $J_y = 0$ in Fig. 1(a), which is a series of uniform chains coupled in the y direction only through the non-Hermitian SSH chain at the center. Notably, although the scattering center is a non-Hermitian SSH chain embedded in the simple 2D square lattice, good quality helical dynamics can be observed in the numerical simulations, which are shown in Fig. B2 in the Appendix B. It is better to choose large site number in the y direction because that the SSH chain is more close to the SSH ring under large site number limitation.

VI. SUMMARY

In summary, we propose the helical transport controlled by a $\mathcal{PT}$-symmetric non-Hermitian SSH ring at the EP as a helical filter. The filter has a chiral coalescence state due to the chirality of EP; therefore, the filter only ensures the resonant transmission for the incidence possessing an identical helicity with it. For the incidence possessing an opposite helicity with the filter, except for a full transmission; additional amplified transmission possessing identical helicity and reflections possessing opposite helicity with the filter are stimulated. The transmissions with opposite helicities interfere and create an interference pattern, which depends on the velocity of the

incidence. We first propose a helical incidence dependent scattering and discuss the multiple-channel scattering problem in a two-dimensional non-Hermitian square lattice. The non-Hermitian SSH ring as a helical filter purifies the excitation: the amplified component in the transmission possesses identical helicity with the filter and can be dominates, associated with a reflection of opposite helicity. Our findings provide an application of the non-Hermitian SSH system and are valuable for the design of optical device using non-Hermitian metamaterial.

APPENDIX

A. Bethe ansatz solution

In this Appendix, we present the derivations of the scattering solutions in Eqs. (9) and (10), which is the heart of this work. We first focus on the scattering solutions of the Hamiltonian in Eq. (8). The Bethe ansatz wave function of a scattering state $|\psi_{k_x}\rangle$ has the form

$$|\psi_{k_x}\rangle = \sum_{j=-\infty}^{\infty} \left(f_j^{\alpha} \, |j, \pi/2\rangle_{\alpha} + f_j^{\beta} \, |j, \pi/2\rangle_{\beta} \right). \tag{A1}$$

The Schrödinger equation $H_{\pi/2} \, |\psi_{k_x}\rangle = E_{k_x} \, |\psi_{k_x}\rangle$ gives

$$\begin{aligned} J_x \left(f_{j-1}^{\alpha} + f_{j+1}^{\alpha} \right) &= E_{k_x} f_j^{\alpha}, j \neq 0, \\ J_x \left(f_{j-1}^{\beta} + f_{j+1}^{\beta} \right) &= E_{k_x} f_j^{\beta}, j \neq 0, \\ J_x f_1^{\alpha} + J_x f_{-1}^{\alpha} + 2\,(w-v)\, f_0^{\beta} &= E_{k_x} f_0^{\alpha}, \\ J_x \left(f_1^{\beta} + f_{-1}^{\beta} \right) &= E_{k_x} f_0^{\beta}. \end{aligned} \tag{A2}$$

Considering an incident plane wave with momentum k_x incoming from one side of lead α, the ansatz wave function $f_j^{\alpha/\beta}$ has the form

$$\begin{aligned} f_j^{\alpha} &= \begin{cases} e^{ik_x j} + r_{k_x}^{\alpha} e^{-ik_x j}, & j \leqslant -1 \\ t_{k_x}^{\alpha} e^{ik_x j}, & j \geqslant 0 \end{cases}, \\ f_j^{\beta} &= \begin{cases} r_{k_x}^{\beta} e^{-ik_x j}, & j \leqslant -1 \\ t_{k_x}^{\beta} e^{ik_x j}, & j \geqslant 0 \end{cases}. \end{aligned} \tag{A3}$$

Here $r_{k_x}^{\alpha/\beta}$ and $t_{k_x}^{\alpha/\beta}$ are the reflection and transmission amplitudes of the incident wave. Substituting Eq. (A3) into Eq. (A2), we obtain the energy

$$E_{k_x} = 2J_x \cos k_x, \tag{A4}$$

and the reflection and transmission amplitudes

$$\begin{aligned} t_{k_x}^{\alpha} &= 1, r_{k_x}^{\alpha} = 0, \\ t_{k_x}^{\beta} &= r_{k_x}^{\beta} = 0. \end{aligned} \tag{A5}$$

Then the scattering wave function is

$$|\psi_{k_x}^{L}\rangle = \sum_{j=-\infty}^{\infty} e^{ik_x j} \, |j, \pi/2\rangle_{\alpha}. \tag{A6}$$

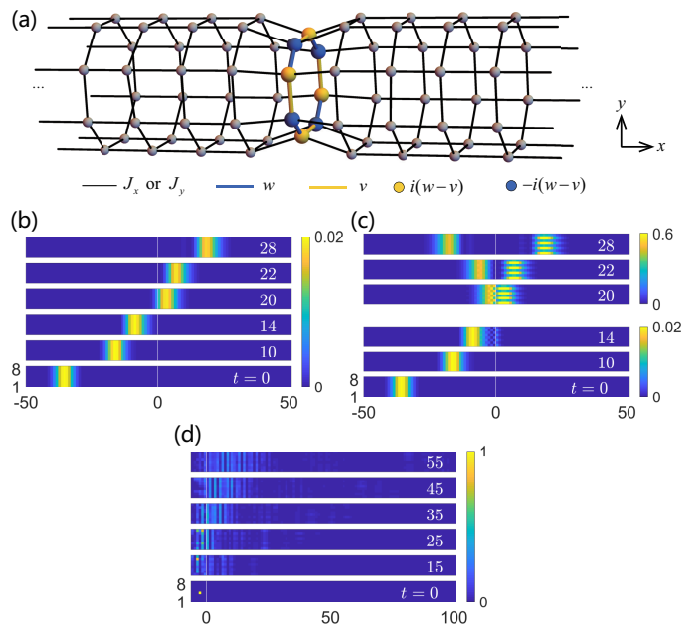

FIG. B1. (a) Non-Hermitian lattice tube with $M = 4$. Snapshots of the intensity at various time moments for three typical initial excitations: (b) Perfect transmission of Gaussian profile $|\Psi_{\mathrm{G}}^{-}(0)\rangle$ with identical helicity of the filter; (c) interfered transmission of Gaussian profile $|\Psi_{\mathrm{G}}^{+}(0)\rangle$ with opposite helicity of the filter; (d) purification and amplification of the single-site excitation. The interference pattern in (c) is in accords with the result in Eq. (11), containing four light and four dark spots. Other parameters of the initial excitation and system are identical with the $M = 2$ case in Figs. 4 and 7.

For the case of an incident plane wave with momentum k_x incoming from one side of lead β, we set $f_j^{\alpha/\beta}$ as the form

$$\begin{aligned} f_j^{\alpha} &= \begin{cases} r_{k_x}^{\alpha} e^{-ik_x j}, & j \leqslant -1 \\ t_{k_x}^{\alpha} e^{ik_x j}, & j \geqslant 0 \end{cases}, \\ f_j^{\beta} &= \begin{cases} e^{ik_x j} + r_{k_x}^{\beta} e^{-ik_x j}, & j \leqslant -1 \\ t_{k_x}^{\beta} e^{ik_x j}, & j \geqslant 0 \end{cases}. \end{aligned} \tag{A7}$$

Substituting it into Eq. (A2), we obtain the energy $E_{k_x} = 2J_x \cos k_x$ and the reflection and transmission amplitudes

$$\begin{aligned} r_{k_x}^{\alpha} &= t_{k_x}^{\alpha} = \frac{(w-v)i}{J_x \sin k}, \\ r_{k_x}^{\beta} &= 0, t_{k_x}^{\beta} = 1. \end{aligned} \tag{A8}$$

Then the scattering wave function is

$$|\psi_{k_x}^{R}\rangle = \sum_{j=-\infty}^{\infty} \left[\frac{(w-v)i}{J_x \sin k_x} e^{ik_x |j|} \, |j, \pi/2\rangle_{\alpha} + e^{ik_x j} \, |j, \pi/2\rangle_{\beta} \right], \tag{A9}$$

After applies the inverse transformation of Eq. (7), the above two scattering solutions Eqs. (A6) and (A9) can

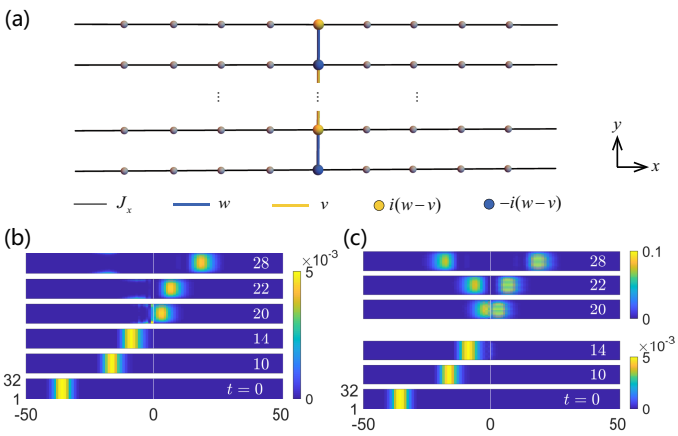

FIG. B2. (a) Schematic of the non-Hermitian 2D square lattice. Snapshots of the intensity at various time moments for two typical initial excitations in the 2D square lattice with $M = 16$. (b) Perfect transmission of Gaussian profile $\left|\Psi_{\mathrm{G}}^{-}(0)\right\rangle$ with identical helicity of the filter; (c) interfered transmission of Gaussian profile $\left|\Psi_{\mathrm{G}}^{+}(0)\right\rangle$ with opposite helicity of the filter. Other parameters are $\alpha_{\mathrm{w}} = 0.3$, $k_x = -\pi/2$ and $N_{\mathrm{c}} = -35$ for the initial excitation and $J_x = 0.25$, $w = 1.5$, $v = 0.5$ for the system. The unit of time is J_x^{-1}.

be written as

$$\left|\psi_{k_x}^{L}\right\rangle = \frac{1}{\sqrt{2}} \sum_{j=-\infty}^{\infty} e^{ik_x j} \left(|j, \pi/2\rangle_1 - |j, \pi/2\rangle_0\right), \quad \text{(A10)}$$

and

$$\left|\psi_{k_x}^{R}\right\rangle = \frac{-i}{\sqrt{2}} \sum_{j=-\infty}^{\infty} \left[e^{ik_x j} \left(|j, \pi/2\rangle_1 + |j, \pi/2\rangle_0\right)\right] - \frac{w-v}{J_x \sin k_x} e^{ik_x |j|} \left(|j, \pi/2\rangle_1 - |j, \pi/2\rangle_0\right)], \quad \text{(A11)}$$

in the space of Hamiltonian Eq. (6). Applying the inverse Fourier transformations with $k_y = \pi/2$, we obtain the solutions in real space

$$\left|\psi_{k_x}^{L}\right\rangle = \frac{-i}{\sqrt{2M}} \sum_{j=-\infty}^{\infty} \sum_{l=1}^{M} (-1)^l e^{ik_x j} \left(|j, 2l-1\rangle - i\,|j, 2l\rangle\right), \quad \text{(A12)}$$

and

$$\left|\psi_{k_x}^{R}\right\rangle = \frac{-1}{\sqrt{2M}} \sum_{j=-\infty}^{\infty} \sum_{l=1}^{M} (-1)^l [e^{ik_x j} \left(|j, 2l-1\rangle + i\,|j, 2l\rangle\right) - \frac{w-v}{J_x \sin k_x} e^{ik_x |j|} \left(|j, 2l-1\rangle - i\,|j, 2l\rangle\right)]. \quad \text{(A13)}$$

B. Numerical results for tube with $M = 4$ and square lattice with $M = 16$

In Fig. B1, we present the numerical simulations for the non-Hermitian lattice tube with size $M = 4$. The dynamics of perfect transmission, interfered transmission, and purification and amplification for single-site excitation are shown.

In Fig. B2, we present the numerical simulations for the non-Hermitian 2D square lattice with size $M = 16$. The dynamics of perfect transmission and interfered transmission are shown.

ACKNOWLEDGMENTS

We acknowledge the support of National Natural Science Foundation of China (Grants No. 11874225, No. 11975128, and No. 11605094).

[1] L. Feng, R. El-Ganainy, and L. Ge, Non-Hermitian photonics based on parity–time symmetry, Nat. Photo. **11**, 752 (2017).
[2] S. Longhi, Parity-time symmetry meets photonics: A new twist in non-Hermitian optics, Europhys. Lett. **120**, 64001 (2017).
[3] R. El-Ganainy, K. G. Makris, M. Khajavikhan, Z. H. Musslimani, S. Rotter, and D. N. Christodoulides, Non-Hermitian physics and $\mathcal{PT}$ symmetry, Nat. Phys. **14**, 11 (2018).
[4] S. K. Gupta, Y. Zou, X.-Y. Zhu, M.-H. Lu, L. Zhang, X.-P. Liu, and Y.-F. Chen, Parity-time Symmetry in Non-Hermitian Complex Media, arXiv:1803.00794.
[5] D. Christodoulides and J. Yang, Parity-time Symmetry and Its Applications (Springer, 2018).
[6] M.-A. Miri and A. Alù, Exceptional points in optics and photonics, Science **363**, eaar7709 (2019).
[7] S. K. Ozdemir, S. Rotter, F. Nori, L. Yang, Parity-time symmetry and exceptional points in photonics, Nat. Mat. **18**, 783 (2019).
[8] Z. H. Musslimani, K. G. Makris, R. El-Ganainy, and D. N. Christodoulides, Optical Solitons in PT Periodic Potentials, Phys. Rev. Lett. **100,** 030402 (2008).
[9] K. G. Makris, R. El-Ganainy, D. N. Christodoulides, and Z. H. Musslimani, Beam Dynamics in PT Symmetric Optical Lattices, Phys. Rev. Lett. **100,** 103904 (2008).
[10] S. Klaiman, U. Günther, and N. Moiseyev, Visualization of Branch Points in PT-Symmetric Waveguides, Phys. Rev. Lett. **101**, 080402 (2008).
[11] Y. D. Chong, L. Ge, H. Cao, and A. D. Stone, Coherent perfect absorbers: time-reversed lasers, Phys. Rev. Lett. **105,** 053901 (2010).
[12] C. E. Rüter, K. G. Makris, R. El-Ganainy, D. N. Christodoulides, M. Segev, and D. Kip, Observation of parity-time symmetry in optics, Nat. Phys. **6,** 192 (2010).
[13] A. Regensburger, C. Bersch, M.-A. Miri, G. Onishchukov, D. N. Christodoulides, and U. Peschel, Parity-time synthetic photonic lattices, Nature **488**, 167 (2012).

[14] L. Feng, Y. Xu, W. S. Fegadolli, M. Lu, J. E. B. Oliveira, V. R. Almeida, Y. Chen, and A. Scherer, Experimental demonstration of a unidirectional reflectionless parity-time metamaterial at optical frequencies, Nature Mater. **12,** 108 (2013).

[15] S. Longhi, Half-spectral unidirectional invisibility in non-Hermitian periodic optical structures, Opt. Lett. **40**, 5694 (2015).

[16] R. Fleury, D. Sounas, and A. Alù, An invisible acoustic sensor based on parity-time symmetry, Nat. Commun. **6**, 5905 (2015).

[17] C. M. Bender, Making sense of non-Hermitian Hamiltonians, Rep. Prog. Phys. **70**, 947 (2007).

[18] N. Moiseyev, Non-Hermitian Quantum Mechanics (Cambridge Univ. Press, 2011).

[19] A. Ruschhaupt, F. Delgado, and J. G. Muga, Physical realization of PT-symmetric potential scattering in a planar slab waveguide, J. Phys. A **38**, L171 (2005).

[20] R. El-Ganainy, K. G. Makris, D. N. Christodoulides, and Z. H. Musslimani, Theory of coupled optical $\mathcal{PT}$-symmetric structures, Opt. Lett. **32,** 2632 (2007).

[21] A. Guo, G. J. Salamo, D. Duchesne, R. Morandotti, M. Volatier-Ravat, V. Aimez, G. A. Siviloglou, and D. N. Christodoulides, Observation of $\mathcal{PT}$-Symmetry Breaking in Complex Optical Potentials, Phys. Rev. Lett. **103,** 093902 (2009).

[22] H. Jing, S. K. Özdemir, Xin-You Lü, J. Zhang, L. Yang, and F. Nori, PT-Symmetric Phonon Laser, Phys. Rev. Lett. **113,** 053604 (2014).

[23] B. Peng, . K. zdemir, F. Lei, F. Monifi, M. Gianfreda, G. L. Long, S. Fan, F. Nori, C. M. Bender, and L. Yang, Parity–time-symmetric whispering-gallery microcavities, Nat. Phys. **10,** 394 (2014).

[24] L. Chang, X. Jiang, S. Hua, C. Yang, J. Wen, L. Jiang, G. Li, G. Wang, and M. Xiao, Parity–time symmetry and variable optical isolation in active–passive-coupled microresonators, Nature Photon. **8,** 524 (2014).

[25] L. Feng, Z. J. Wong, R.-M. Ma, Y. Wang, and X. Zhang, Single-mode laser by parity-time symmetry breaking, Science **346,** 972 (2014).

[26] H. Hodaei, M.-A. Miri, M. Heinrich, D. N. Christodoulides, and M. Khajavikhan, Parity-time–symmetric microring lasers, Science **346,** 975 (2014).

[27] J. G. Muga, J. P. Palaob, B. Navarroa, and I. L. Egusquizac, Complex absorbing potentials, Phys. Rep. **395**, 357 (2004).

[28] F. Cannata, J-P. Dedonder, and A. Ventura, Scattering in $\mathcal{PT}$-symmetric quantum mechanics, Ann. Phys. **322**, 397 (2007).

[29] Z. Ahmed, Reciprocity and unitarity in scattering from a non-Hermitian complex $\mathcal{PT}$-symmetric potential, Phys. Lett. A **377,** 957 (2013).

[30] A. Mostafazadeh, Generalized unitarity and reciprocity relations for-symmetric scattering potentials, J. Phys. A: Math. Theor. **47,** 505303 (2014).

[31] X. Z. Zhang and Z. Song, Momentum-independent reflectionless transmission in the non-Hermitian time-reversal symmetric system, Ann. Phys. **339,** 109 (2013).

[32] S. Longhi, D. Gatti and G. D. Valle, Robust light transport in non-Hermitian photonic lattices, Sci. Rep. **5**, 13376 (2015).

[33] S. Longhi, D. Gatti, and G. D. Valle, Non-Hermitian transparency and one-way transport in low-dimensional lattices by an imaginary gauge field, Phys. Rev. B **92**, 094204 (2015).

[34] X. Q. Li, X. Z. Zhang, G. Zhang, and Z. Song, Asymmetric transmission through a flux-controlled non-Hermitian scattering center, Phys. Rev. A. **91,** 032101 (2015).

[35] S. Longhi, Non-reciprocal transmission in photonic lattices based on unidirectional coherent perfect absorption, Opt. Lett. **40,** 1278 (2015).

[36] L. Jin, X. Z. Zhang, G. Zhang, and Z. Song, Reciprocal and unidirectional scattering of parity-time symmetric structures, Sci. Rep. **6**, 20976 (2016).

[37] L. Jin, P. Wang, and Z. Song, Unidirectional perfect absorber, Sci. Rep. **6**, 32919 (2016).

[38] C. Li, L. Jin, and Z. Song, Non-Hermitian interferometer: Unidirectional amplification without distortion, Phys. Rev. A **95**, 022125 (2017).

[39] L. Jin, P. Wang, and Z. Song, One-way light transport controlled by synthetic magnetic fluxes and-symmetric resonators, New J. Phys. **19**, 015010 (2017).

[40] L. Jin and Z. Song, Incident Direction Independent Wave Propagation and Unidirectional Lasing, Phys. Rev. Lett. **121**, 073901 (2018).

[41] S. Longhi, Non-Hermitian topological phase transition in PT-symmetric mode-locked lasers, Opt. Lett. **44**, 1190 (2019).

[42] A. Metelmann and A. A. Clerk, Nonreciprocal Photon Transmission and Amplification via Reservoir Engineering, Phys. Rev. X **5**, 021025 (2015).

[43] H. Ramezani, P. K. Jha, Y. Wang, and X. Zhang, Nonreciprocal Localization of Photons, Phys. Rev. Lett. **120**, 043901 (2018).

[44] T. T. Koutserimpas and R. Fleury, Nonreciprocal Gain in Non-Hermitian Time-Floquet Systems, Phys. Rev. Lett. **120**, 087401 (2018).

[45] R. Huang, A. Miranowicz, J.-Q. Liao, F. Nori, and H. Jing, Nonreciprocal Photon Blockade, Phys. Rev. Lett. **121**, 153601 (2018).

[46] B. Midya, H. Zhao, and L. Feng, Non-Hermitian photonics promises exceptional topology of light, Nat. Commun. **9**, 2674 (2018).

[47] C. Poli, M. Bellec, U. Kuhl, F. Mortessagne, and H. Schomerus, Selective enhancement of topologically induced interface states in a dielectric resonator chain, Nat. Commun. **6**, 6710 (2015).

[48] S. Weimann, M. Kremer, Y. Plotnik, Y. Lumer, S. Nolte, K. G. Makris, M. Segev, M. C. Rechtsman, and A. Szameit, Topologically protected bound states in photonic parity–time-symmetric crystals, Nat. Mater. **16**, 433 (2017).

[49] M. Pan, H. Zhao, P. Miao, S. Longhi, and L. Feng, Photonic zero mode in a non-Hermitian photonic lattice, Nat. Commun. **9**, 1308 (2018).

[50] P. St-Jean, V. Goblot, E. Galopin, A. Lemaître, T. Ozawa, L. Le Gratiet, I. Sagnes, J. Bloch, and A. Amo, Lasing in topological edge states of a one-dimensional lattice, Nat. Photon. **11**, 651 (2017).

[51] H. Zhao, P. Miao, M. H. Teimourpour, S. Malzard, R. El-Ganainy, H. Schomerus, and L. Feng, Topological hybrid silicon microlasers, Nat. Commun. **9**, 981 (2018).

[52] M. Parto, S. Wittek, H. Hodaei, G. Harari, M. A. Bandres, J. Ren, M. C. Rechtsman, M. Segev, D. N. Christodoulides, and M. Khajavikhan, Edge-Mode Lasing in 1D Topological Active Arrays, Phys. Rev. Lett. **120**, 113901 (2018).

[53] B. X. Wang and C. Y. Zhao, Topological phonon polaritons in one-dimensional non-Hermitian silicon carbide nanoparticle chains, Phy. Rev. B **98**, 165435 (2018); Topological photonic states in one-dimensional dimerized ultracold atomic chains, Phy. Rev. A **98**, 023808 (2018).

[54] S. Longhi, Bloch oscillations and Wannier-Stark localization in a tight-binding lattice with increasing intersite coupling, Phys. Rev. B **80**, 033106 (2009).

[55] G. Corrielli, G. Della Valle, A. Crespi, R. Osellame, and S. Longhi, Observation of Surface States with Algebraic Localization, Phys. Rev. Lett. **111**, 220403 (2013).

[56] W. D. Heiss and H. L. Harney, The chirality of exceptional points, Eur. Phys. J. D **17**, 149 (2001).

[57] K. Ding, G. Ma, M. Xiao, Z. Q. Zhang, and C. T. Chan, Emergence, Coalescence, and Topological Properties of Multiple Exceptional Points and Their Experimental Realization, Phys. Rev. X **6**, 021007 (2016).

[58] L. Jin, Parity-time-symmetric coupled asymmetric dimers, Phys. Rev. A **97**, 012121 (2018).

[59] L. Jin and Z. Song Bulk-boundary correspondence in a non-Hermitian system in one dimension with chiral inversion symmetry, Phys. Rev. B **99**, 081103(R) (2019).

[60] K. L. Zhang, H. C. Wu, L. Jin, and Z. Song, Topological Phase Transition Independent of System Non-Hermiticity, Phys. Rev. B **100**, 045141 (2019).

[61] N. Hatano and D. R. Nelson, Localization transitions in non-Hermitian quantum mechanics, Phys. Rev. Lett. **77,** 570 (1996); Vortex pinning and non-Hermitian quantum mechanics, Phys. Rev. B **56,** 8651 (1997).

[62] S. Longhi, Bound states in the continuum in PT-symmetric optical lattices, Opt. Lett. **39**, 1697 (2014).

[63] M. Hafezi, Measuring Topological Invariants in Photonic Systems, Phys. Rev. Lett. **112**, 210405 (2014); M. Hafezi, Synthetic gauge fields with photons, Int. J. Mod. Phys. B **28**, 1441002 (2014).

[64] S. Longhi, Topological Phase Transition in non-Hermitian Quasicrystals, Phys. Rev. Lett. **122**, 237601 (2019).

[65] H. Jiang, L.-J. Lang, C. Yang, S.-L. Zhu, and S. Chen, Interplay of non-Hermitian skin effects and Anderson localization in non-reciprocal quasiperiodic lattices, Phys. Rev. B **100**, 054301 (2019).

[66] S. Longhi, Metal-insulator phase transition in a non-Hermitian Aubry-Andre-Harper Model, arXiv:1908.03371.

[67] C. H. Lee and R. Thomale, Anatomy of skin modes and topology in non-Hermitian systems, Phys. Rev. B **99**, 201103(R) (2019).

[68] S. Longhi, Probing non-Hermitian skin effect and non-Bloch phase transitions, Phys. Rev. Research **1**, 023013 (2019).

[69] T. Helbig, T. Hofmann, S. Imhof, M. Abdelghany, T. Kiessling, L. W. Molenkamp, C. H. Lee, A. Szameit, M. Greiter, and R. Thomale, Observation of bulk boundary correspondence breakdown in topolectrical circuits, arXiv:1907.11562.

[70] T. Hofmann, T. Helbig, F. Schindler, N. Salgo, M. Brzezińska, M. Greiter, T. Kiessling, D. Wolf, A. Vollhardt, A. Kabaši, C. H. Lee, A. Bilušić, R. Thomale, and T. Neupert, Reciprocal skin effect and its realization in a topolectrical circuit, arXiv:1908.02759.